Digital pulse-shape discrimination of fast neutrons and γ rays

P.-A. Söderström [a,*], J. Nyberg [a], R. Wolters [a]

[a] *Department of Physics and Astronomy, Uppsala University, SE-75121 Uppsala, Sweden*

Abstract

Discrimination of the detection of fast neutrons and γ rays in a liquid scintillator detector has been investigated using digital pulse-processing techniques. An experimental setup with a ^{252}Cf source, a BC-501 liquid scintillator detector, and a BaF_2 detector was used to collect waveforms with a 100 Ms/s, 14 bit sampling ADC. Three identical ADC's were combined to increase the sampling frequency to 300 Ms/s. Four different digital pulse-shape analysis algorithms were developed and compared to each other and to data obtained with an analogue neutron-γ discrimination unit. Two of the digital algorithms were based on the charge comparison method, while the analogue unit and the other two digital algorithms were based on the zero-crossover method. Two different figure-of-merit parameters, which quantify the neutron-γ discrimination properties, were evaluated for all four digital algorithms and for the analogue data set. All of the digital algorithms gave similar or better figure-of-merit values than what was obtained with the analogue setup. A detailed study of the discrimination properties as a function of sampling frequency and bit resolution of the ADC was performed. It was shown that a sampling ADC with a bit resolution of 12 bits and a sampling frequency of 100 Ms/s is adequate for achieving an optimal neutron-γ discrimination for pulses having a dynamic range for deposited neutron energies of 0.3-12 MeV. An investigation of the influence of the sampling frequency on the time resolution was made. A FWHM of 1.7 ns was obtained at 100 Ms/s.

Key words: Digital pulse-shape discrimination, fast-neutron detection, liquid scintillator, BC-501, sampling ADC
PACS:

* Corresponding author
Email addresses: Par-Anders.Soderstrom@fysast.uu.se (P.-A. Söderström), Johan.Nyberg@fysast.uu.se (J. Nyberg).

1 Introduction

In experimental studies of the structure of exotic nuclides far from the line of β stability, it is important to accurately and efficiently identify the residual nuclides produced in the nuclear reactions. One of the most common type of reactions used is heavy-ion fusion-evaporation, in which two nuclei fuse to form a compound nucleus, which decays by evaporating a number of light particles, mainly neutrons, protons, and/or α particles.

The exotic nuclides of interest are produced with very small cross sections in this type of reactions. A usual method of identifying the proton (Z) and neutron (N) number of these nuclides, is to detect the type and number of emitted light particles. If all emitted particles are detected in each reaction, the final nuclide can uniquely be identified by subtracting the sum of the Z and N of the emitted particles from the Z and N of the compound nucleus, With careful analysis of the distributions of the number of detected light particles, it is possible to identify the Z and N of the residual nuclides even if all emitted particles are not detected in every reaction, which usually is the case.

The light charged particles are usually detected by a highly efficient Si or CsI detector array, while the neutrons are detected by an array of liquid scintillator detectors. The requested nuclear structure information is obtained by using a high-resolution γ-ray spectrometer for detection of the emitted γ rays in coincidence with the light particles.

A clean and efficient detection of the number of emitted neutrons in each reaction, is of utmost importance for studies of nuclides located close to the proton-drip line. The compound nuclei created in such studies decay mainly by emission of a number of protons, which brings the Z of the final nucleus closer to the β-stability line. Only very rarely are neutrons emitted and by detecting them one can identify the neutron number of the produced rare exotic nuclides. One of the major challenges of the detection of these rare neutrons, is to discriminate between neutrons and other particles, mainly γ rays, which are also registered by the neutron detectors.

Future studies of exotic nuclei will mainly be performed by using reactions induced by radioactive instead of stable heavy ions. This allows for a production of compound nuclei located even further from the line of β stability. Experiments with radioactive ion beams are often hampered by the high γ-ray background radiation originating from the decay of the radioactive beam. Neutron detector arrays, to be used in future experiments with high-intensity radioactive ion beams, for example at the HISPEC [1] and DESPEC [2] setups at NuSTAR/FAIR [3,4] and at SPIRAL-2 [5], must therefore be designed to cope with such a highly increased γ-ray background. Another future appli-

cation is experiments with extremely high-intensity stable beams, which also generate intense background radiation, leading to problems of clean neutron detection due to random and pileup effects.

The need for efficient neutron detection is not only required in heavy-ion fusion-evaporation reactions close to the proton drip-line, but also e.g. as "veto" detectors in studies of neutron-rich nuclei and in neutron spectroscopy and neutron correlation studies of neutron-halo nuclei.

This paper presents a study of the discrimination of the detection of neutrons, with energies from about 0.3 MeV to 10 MeV, from γ rays in a liquid scintillator detector using a fast sampling analogue-to-digital converter (ADC) and digital pulse-processing techniques. Several different digital neutron-γ discrimination (NGD) algorithms were implemented and the discrimination quality was compared with what could be achieved with an analogue system. For the digital versions, the discrimination properties were studied as a function of sampling frequency and bit resolution of the ADC. The main focus of the study is on the detection of pulses corresponding to low energy deposition in the detector, since in this case the NGD is more difficult and the needs for improvements are larger.

Section 2 is a brief introduction to the principle of pulse-shape discrimination in liquid scintillators. The details of the performed experiment are presented in section 3, the implemented digital pulse-shape algorithms in section 4, and the analysis and results in section 5.

Preliminary results of this work have been published in [6].

2 Liquid scintillators and pulse-shape discrimination

In order to get a good and clean detection of fast neutrons, several features of the detector design needs to be taken into consideration. The organic liquid scintillator, which is a so called proton recoil detector, has been used very successfully in previous neutron detector arrays [7,8,9]. This is partly because of its good efficiency for detection of fast neutrons, which is due to the large cross section for elastic neutron-proton scattering, and partly because of its excellent pulse-shape discrimination (PSD) properties, which allows for a discrimination of neutrons and γ rays.

A possible problem of using a detector, which is based on elastic neutron-proton scattering, is that the neutron will have a substantial kinetic energy after the interaction and a velocity in some random direction. In a closely-packed detector array, multiple scattering between different segments becomes

a problem, which can cause quite severe errors in counting the number of neutrons emitted in each reaction. Methods to correct for this have been developed with good results [10,11]. This requires, however, very good discrimination of neutrons and γ rays, since it has been shown that even a small amount of γ rays mis-interpreted as neutrons dramatically reduces the quality of the multiple-scattering rejection [11].

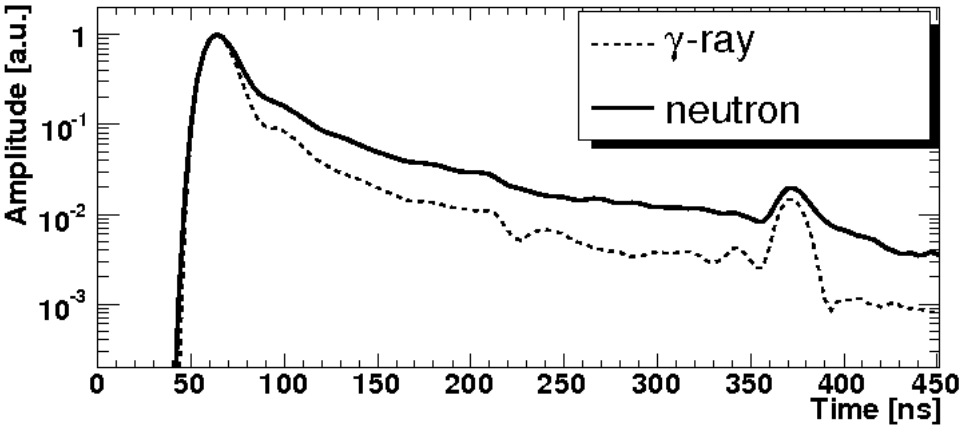

Fig. 1. Pulse shapes from a BC-501 liquid scintillator detector measured with a fast sampling ADC, as described in section 3. The pulses are averaged over about 70 000 γ-ray pulses and 40 000 neutron pulses and normalized to 1.

The problem of discriminating between neutron and γ-ray interactions in liquid scintillators by using analogue electronics is well studied. Several methods exist to accomplish this, for example by measuring the zero-crossover (ZCO) time of a shaped pulse [16,17] or by comparing the charge collected from different parts of the pulse [18]. The performance of these methods with respect to each other is also well known in the analogue case [19]. With fast sampling ADC's becoming better and available at smaller costs, new advanced algorithms for NGD have been developed and used with very good results. A correlations approach [20], a curve fitting method [21] and a pulse gradient method [22,23] have for example all yielded good results regarding the discrimination of neutrons and γ rays.

3 Experiment

The experiment was carried out using a liquid scintillator detector from the NORDBALL neutron detector array [7], a BaF_2 detector for triggering and time reference, and a ^{252}Cf source.

The scintillator liquid of the neutron detector was of type BC-501 [12]. The

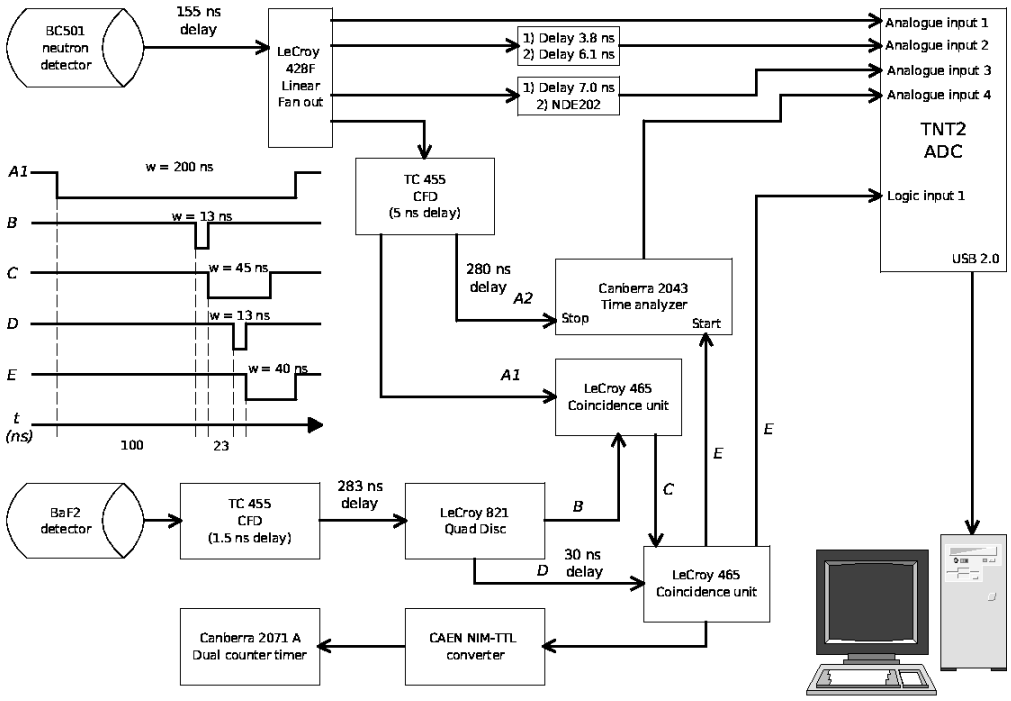

Fig. 2. Schematic electronics block and timing diagrams of the setup used in this work. The delay units consist of coaxial cables of type RG58 (delays > 10 ns) or RG174. The signals shown in the timing diagram correspond to the detection of prompt γ rays in the two detectors. 1) 300 Ms/s and 2) 200 Ms/s setup.

liquid was contained in a 3.3 litre hexagonal aluminium can and it was viewed through a glass window by a 14-stage, 5" diameter PMT of type Philips XP2041. This PMT is designed to run optimally at about 2200 V. In this experiment it was run at 1750 V, in order to increase the energy range of the pulses from the anode output which could be sampled by the ADC without being saturated. The trigger and time reference detector was a 2"$\times$2" BaF_2 scintillator with a Philips XP2020Q PMT.

The ^{252}Cf source consisted of several weak sources placed in a plastic container of cylindrical shape (diameter 1.5 cm, length 6 cm, wall thickness 2 mm). The radioactive material of the source was distributed over a volume of about 1 cm^3. The source had a total activity of about 200 kBq, which implies an emission of about $2 \cdot 10^4$ neutrons and $6 \cdot 10^4$ γ rays per second. The source was placed between the two detectors, with a distance of 2 cm and 75 cm from the front of the BaF_2 and BC-501 detectors, respectively.

Schematic block and timing diagrams of the electronics setup are shown in fig. 2. The anode output of the neutron detector was connected to a LeCroy 428F linear fan-out (LFO). A reflection of the signal between the anode output and the LFO was observed. This effect was due to a non-optimal design of the voltage divider regarding impedance matching and it led to a distortion of

the signal pulse shapes. This problem was solved by introducing a $\approx$ 30 m long RG58 coaxial cable between the anode output and the LFO input. The reflection and distorted part of the signal was thus delayed by about 300 ns and appeared outside the range used for the pulse-shape analysis. The reflection is clearly seen in fig. 1 in the time range 360 to 390 ns. The long RG58 cable also made the conditions more similar to real physics experiment, in which the detector and the electronics usually are separated by large distances. This caused an increase in the pulse rise time (10 % to 90 %), from 6.5 ns before the cable, to 7 ns afterwards.

One of the LFO outputs and the anode signal of the BaF_2 detector were sent to constant fraction discriminators (CFD) of type TC 455. The threshold of the BC-501 CFD was set to 22 keV for electrons which corresponds to 310 keV for recoil protons. The threshold of the BaF_2 CFD was set to a rather high value to reject signals from X rays, low energy γ rays and noise.

The outputs of the two CFD units were sent to the inputs of a LeCroy 465 coincidence unit (signals A and B in fig. 2), in which an overlap coincidence between the signals in the BC-501 and BaF_2 detectors was created. The second LeCroy 465 unit in fig. 2 (signal inputs C and D) made sure that the leading edge of the output signal E always was determined by the BaF_2 detector. Signal E was finally used as a trigger of the sampling ADC (logic input 1) and as a start of the time-to-amplitude converter (TAC). The TAC was stopped by the delayed BC-501 signal A2 and measured the time-of-flight (TOF) difference between the detected γ rays and neutrons in the detectors.

The anode signal of the BC-501 detector was digitized by a TNT2 ADC unit [24]. The TNT2 is a single width NIM unit and contains four independent channels, each of which has a 14-bit flash ADC with a sampling frequency of 100 megasamples per second (Ms/s), an analogue bandwidth of 40 MHz, and an input range of $\pm$0.62 V when terminated in 50Ω. The TNT2 is set up, controlled and read out by a Linux PC via a USB 2.0 interface. A Java graphical user interface is used for control and monitoring of the unit. In this experiment the TNT2 was used in the digital oscilloscope mode, which allows for readout of the digitized waveforms of each of the four channels.

In order to increase the sampling frequency of the ADC from 100 Ms/s to 300 Ms/s, three of the output signals of the LFO were used for pulse sampling. One of the outputs was defined as the zero-delay branch and was connected directly from the LFO to analogue input 1 of the TNT2. The other two outputs were delayed relative to the zero-delay branch using short RG174 cables, before they were fed into analogue inputs 2 and 3 of the TNT2. The total effective delays (cables and internal delays of the LFO and TNT2) of analogue inputs 2 and 3 relative to input 1 were 3.8 ns and 7.0 ns, respectively. This was sufficiently close to the 3.33 ns time difference between samples that would be

the result a true 300 Ms/s ADC. All three sampling channels were gain and time matched against each other using a 1 MHz sine output from an Agilent function generator of model 33250A.

Since the above procedure only effected the digital bandwidth of the sampling system, one of its consequences was that the analogue bandwidth did not match the digital bandwidth. To examine the effects of this, the frequency response of the system was measured. It was found to have a low pass characteristics of order 2.27 and a cut-off frequency of 35.7 MHz. The effect of the analogue bandwidth on the pulse was examined by estimating the shape of an undistorted pulse by correcting a discrete Fourier transformation with the measured frequency response. A comparison between a typical pulse and an estimate of the undistorted version of the same pulse is shown in fig. 3. An increase in the rise time (10 % to 90 %) to 10 ns for the digitized pulses was observed. In the part of the pulse that is most relevant to this work, the region of the fast and slow decay components, the two pulses follow each other very closely. The effects on the rise time, and consequently on the fast component, gives an added amplitude uncertainty of $\lesssim 5$ %. The effects due to the mismatch of the analogue and digital bandwidths did not influence the results obtained in this work.

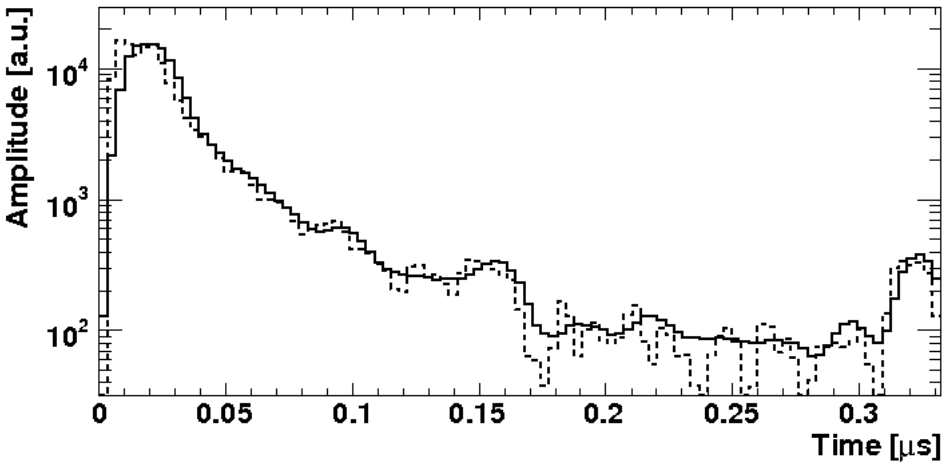

Fig. 3. Effects of the limited analogue bandwidth. A typical measured pulse shape (solid histogram) and the corresponding undistorted pulse shape after correcting for the finite analogue bandwidth (dashed histogram) are shown. To remove artefacts due to the finite size of the discrete Fourier transform, the histograms are smoothed twice using the 353QH algorithm [25].

By utilizing well known analogue PSD electronics, a reference data set was obtained, which could be used for comparisons with the results obtained by the digital PSD algorithms. The analogue PSD unit used in the present work was of type BARTEK NDE202 [26], which was designed and built for the EUROBALL Neutron Wall [8]. This unit has a built in circuit for NGD based

on the ZCO technique. The ZCO information is available from the NDE202 as a TAC output signal, which gives the time difference between the leading edge of the signal, obtained from its internal CFD, and the ZCO signal. The threshold of the internal CFD was set to 68 keV for electrons, corresponding to 600 keV for protons, i.e. to a higher value than the TC 455 CFD used by the BC-501 detector. The ZCO TAC output signal of the NDE202 was sent to analogue input 3 of the TNT2 ADC after being attenuated to be within the amplitude range of the ADC (see fig. 2).

In the experiments which included the analogue PSD unit, only two of the TNT2 analogue inputs could be used for digitization of the BC-501 anode signals, as seen in fig. 2. Identical to what was described above, the LFO output for the zero-delay branch was sent directly to analogue input 1 of the TNT2. Another LFO output was delayed by 6.1 ns relative to the zero-delay branch. In this way a sampling frequency of 200 Ms/s could be achieved.

During the experiments the singles rates were about 2 and 30 kHz for the BC-501 and BaF_2 detectors, respectively. The true and random coincidence rates were about 300 Hz and 0.5 Hz, respectively.

In the experiment two data sets were collected, one with the 300 Ms/s and the other with the 200 Ms/s setup, each containing about 6 million events. The events contained the digitized waveforms of all four channels of the TNT2. The read out waveforms had a length of 20 μs (2000 sampling points) and a starting time about 1.8 μs before the leading edge of the pulses.

A rough energy calibration was obtained by using a ^{137}Cs source. The Compton edge at 480 keV was observed by an oscilloscope at the output of the LFO to have an amplitude of about 0.5 V. Using a sine signal with an amplitude of 500 mV from the Agilent function generator, the ADC could be calibrated with a γ-ray calibration coefficient C_e that converts from pulse amplitude A, measured in channel numbers by the ADC, to electron energy E_e in keV:

$$E_\mathrm{e} = C_\mathrm{e} \cdot A, \quad C_\mathrm{e} = 0.076 \text{ channels/keV}. \tag{1}$$

This amplitude-energy conversion is only valid for γ-ray interactions. The following procedure was followed to get an amplitude-energy conversion for neutron interactions. The number of created scintillation photons per deposited energy is much smaller for proton recoils compared to electrons. The conversion from deposited proton recoil energy E_p in MeV to equivalent electron energy E_ee in MeV was done by using the relation [27]

$$E_\mathrm{ee} = 0.83 \cdot E_\mathrm{p} - 2.82 \cdot \left(1 - \mathrm{e}^{-0.25 \cdot E_\mathrm{p}^{0.93}}\right). \tag{2}$$

This relation holds for the total integrated charge of the measured pulse, which

is proportional to the sum of all created scintillation photons. The total integrated charge of the pulse is proportional to the "area" between the digitized waveform and its baseline, which can be obtained by summing the content of each channel over the whole pulse. An additional correction was made for conversion from pulse amplitude to energy for the neutron interactions. A distribution of the ratio of the total integrated area ($\sim$ total charge) to the amplitude for a large number of pulses with varying amplitudes is shown in fig. 4. Two peaks, corresponding to γ rays and neutrons are clearly visible in

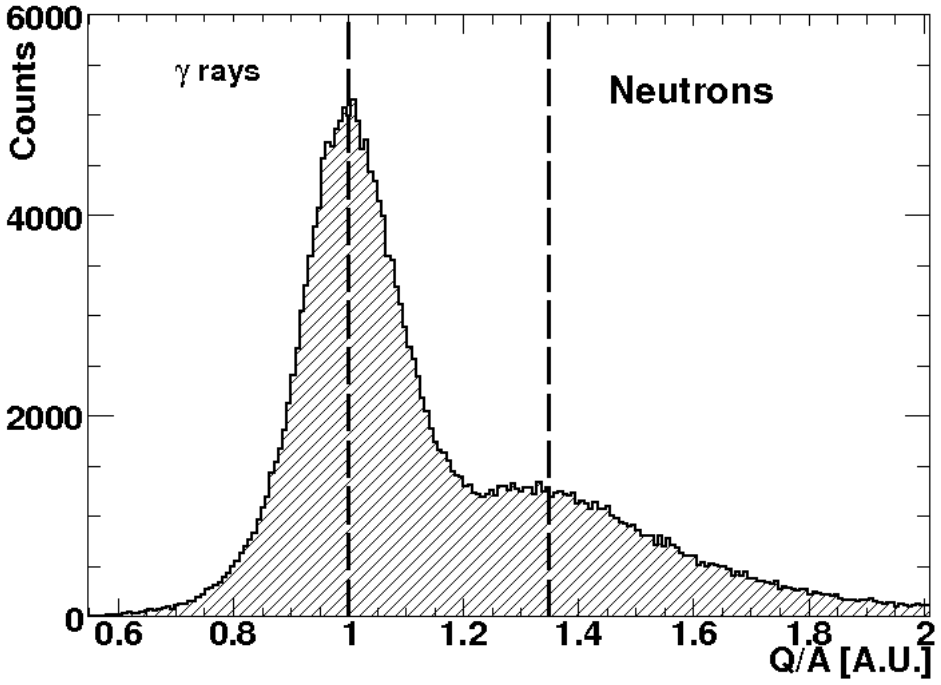

Fig. 4. The ratio of total charge to amplitude for a large number of waveforms of varying amplitude. The ratio for the peak corresponding to γ rays is normalized to unity, which gives a value of 1.35 for the neutron peak.

this plot. The ratio of the position of these peaks is $k = 1.35$, which gives the factor by which a measured amplitude A in channel numbers should be converted to electron equivalent energy E_{ee} for a neutron interaction:

$$E_{\mathrm{ee}} = C_{\mathrm{p}} \cdot A = k \cdot C_{\mathrm{e}} \cdot A = k \cdot E_{\mathrm{e}}, \quad k = \frac{C_{\mathrm{p}}}{C_{\mathrm{e}}}. \tag{3}$$

A conversion from measured amplitude A to proton recoil energy E_{p} can finally be done by combining equations 2 and 3 and solving numerically for E_{p}. All amplitudes given in keV in the rest of this paper correspond to E_{e} and thus have to be translated to E_{p} according to this prescription.

A gain and time matching of the analogue inputs 1-3 of the ADC was done to

correct for any differences in the inputs. This was achieved by feeding a sine wave from the Agilent function generator into the LFO and from there into the TNT2. A few thousand calibration events were collected and a fit of a sine function was made for each channel in each event. From the fits the relative gain and time between the three channels were extracted.

The short and long term stability of the setup regarding changes in the relative gain of the analogue channels of the TNT2 was excellent and did not need any further corrections.

For the real data, obtained with the ^{252}Cf source, the signal baseline of each read out waveform was calculated on an event-by-event basis. This was necessary because the LFO introduced a low frequency noise on the signal waveforms, which was observed as a small instability of the baseline. The position of the baseline was obtained by taking an average of 75 sampling points in a region starting 1.8 μs and ending 1.1 μs before the leading edge of the pulse.

The time information was extracted from the TAC signal. The baseline of this signal was determined for each event as an average before and after the flat top. The flat top itself was then fitted with a constant value, and the time information extracted from this value. See fig. 5 for the obtained TOF distribution.

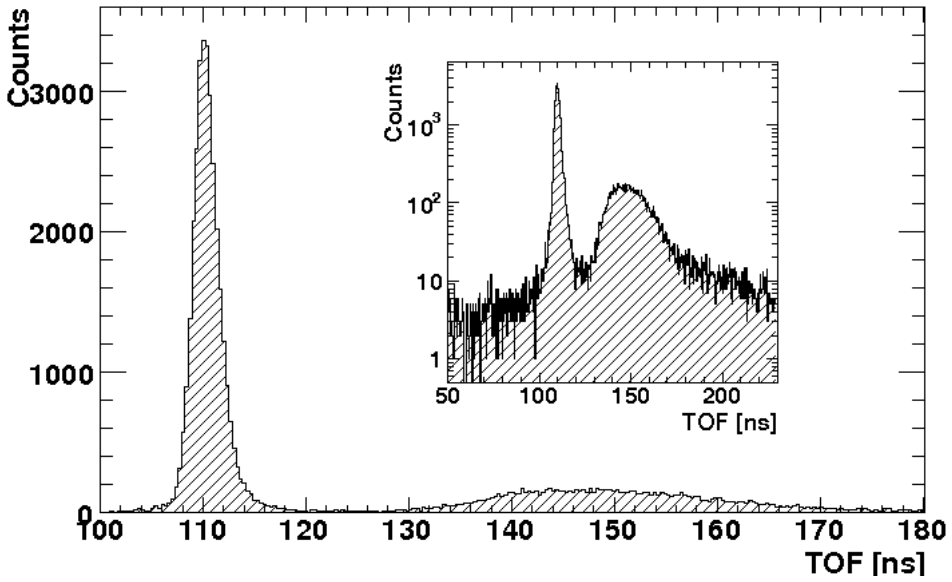

Fig. 5. Measured time-of-flight distribution of pulses with amplitude in the range E_e = 90-700 keV. The γ-ray peak, to the left, has a FWHM of about 3.1 ns. The inset shows the TOF distribution in logarithmic scale.

Table 1
Classification of the PSD algorithms studied in this paper.

Methods	Algorithms		
	Analogue	Digital	Digital
ZCO	NDE202	Convolution	Integrated rise time
CC	-	Slow component	GDM Integral

4 Digital PSD algorithms for neutron-γ discrimination

In order to get the requested information from a PSD analysis an observable, which differs between the interacting particles, is needed. A general way to define such an observable, S, is by the integral

$$S = \int_0^T p(t)w(t)\mathrm{d}t, \tag{4}$$

where T is the time of examination of the pulse $p(t)$ and $w(t)$ is a weighting function with the purpose to enhance the features used for the PSD. The choice of $w(t)$ determines the quality of the discrimination. It has been shown [28] that the theoretically optimal form of $w(t)$ is

$$w(t) = \frac{\bar{n}(t) - \bar{\gamma}(t)}{\bar{n}(t) + \bar{\gamma}(t)}, \tag{5}$$

where $\bar{n}(t)$ and $\bar{\gamma}(t)$ are the average pulse shapes for neutron and γ-ray interactions respectively. The existing analogue PSD algorithms attempt to create a weighting function $w(t)$ in hardware, which is as close as possible to eq. (5). This can be done either directly by finding an analytical expression, which approximates $w(t)$ for the algorithm in use, or indirectly by comparing this expression with the optimal weighting function. See for example Ref. [17] for this kind of analysis of the ZCO method.

The two classes of PSD algorithms implemented digitally in this work are the well known ZCO and charge comparison (CC) methods. These were chosen for their simplicity and since they are known to work well both for analogue and digital PSD systems. The simplicity of the algorithms also makes the required computing power minimal, which is an important parameter for future real-time implementations. The implemented algorithms and the analogue discrimination are listed in table 1.

4.1 Digital leading-edge discriminator

The starting time of the pulse was determined by a simple digital leading-edge discriminator (LED), which was implemented in the following way. The first sampling point of the recorded waveform with an amplitude value larger than a chosen threshold value was identified. The time at which the pulse crossed the threshold was determined by making a linear interpolation between this sampling point and the previous one. No corrections for time walk were made in this work.

4.2 ZCO: Analogue and convolution algorithm

The analogue ZCO method is usually implemented by a shaping of the detector pulse into a bipolar signal, followed by a zero-crossing circuit, which detects the time when the amplitude of the bipolar signal changes polarity, the ZCO time. The shaping can be done by using double delay lines [16] or an RC-CR integrating and differentiating network [17]. The analogue PSD algorithm of the NDE202 unit used in this work contains a bipolar RC-CR shaping amplifier and a zero-crossing detector.

In this work, a digital version of the ZCO method, here named the convolution algorithm, was implemented by imitating a RC-CR network. A digital filter $h(t)$ of length t_L was applied to the raw input pulse $p(t)$ to create the shaped pulse $f(t)$ as the convolution (denoted by $*$) of $p(t)$ and $h(t)$:

$$f(t) = p(t) * h(t) \equiv \sum_{\tau=t-t_L}^{t} p(\tau)h(t-\tau). \tag{6}$$

The filter $h(t)$ is itself composed of a convolution of three filters:

$$h(t) = h_{\mathrm{s}}(t) * h_{\mathrm{i}}(t) * h_{\mathrm{d}}(t). \tag{7}$$

The first filter, $h_{\mathrm{s}}(t)$, is a smoothing function, which averages each sampling point with its neighbours within a time interval τ_{s} and the aim of which was to smooth out the high-frequency noise of the signal. The integrating filter $h_{\mathrm{i}}(t)$ is a digital version of an analogue integrator [14, Ch. 16], which was obtained from the differential equation

$$\frac{\mathrm{d}p_{\mathrm{out}}}{\mathrm{d}t} + \frac{p_{\mathrm{out}}}{\tau_{\mathrm{i}}} = \frac{p_{\mathrm{in}}}{\tau_{\mathrm{i}}} \tag{8}$$

and which has the solution

$$p_{\text{out}} = \mathrm{e}^{-\frac{t}{\tau_{\text{i}}}} \int \mathrm{e}^{\frac{t}{\tau_{\text{i}}}} \frac{p_{\text{in}}}{\tau_{\text{i}}} \mathrm{d}t. \tag{9}$$

Letting $p_{\text{in}} = \delta(t)$, where $\delta(t)$ is the Dirac delta function, and $\tau_{\text{i}} p_{\text{out}} = h_{\text{i}}(t)$, the exponential integration filter becomes

$$h_{\text{i}}(t) = \mathrm{e}^{-\frac{t}{\tau_{\text{i}}}}. \tag{10}$$

Finally the pulse was differentiated with $h_{\text{d}}(t)$, which was a regular numerical differentiator filter, as described in [14, Ch. 17]. The filter $h(t)$ produces a bipolar pulse with a zero crossing, which depends on the type of particle that generated the pulse. The selection of the time constants τ_{s} and τ_{i} was carefully examined and the optimal values for this setup was found to be $\tau_{\text{s}} = 177$ ns and $\tau_{\text{i}} = 600$ ns. These values are similar to the time constants reported to be optimal for an analogue discrimination system [17]. An example of a filtered neutron and γ-ray pulse is shown in fig. 6a.

4.3 ZCO: Integrated rise-time algorithm

By using digital pulse processing it is possible to evaluate the integrated rise time of the pulse directly [30], instead of first shaping it to extract the ZCO time, as explained in the previous subsection. In the integrated rise-time algorithm (IRT) implemented in this work, a mathematical integration filter

$$h(t) = h_{\text{i}}'(t) = \begin{cases} 0, \, t \leq 0 \\ 1, \, t > 0 \end{cases} \tag{11}$$

was used in eq. (6). The rise time of the integrated pulse was then extracted from the time difference between the position in time of the 10 % and 72 % values of the height of the integrated pulse. Its value depends on the type of interacting particle, as illustrated in fig. 6b.

4.4 CC: Slow component algorithm

The slow component algorithm, based on the charge comparison method, is a direct application of eq. 4. The main assumption of this algorithm is that all sampling points in the delayed part of the pulse, corresponding to the slow component of the scintillation light, have equal weights. This was implemented

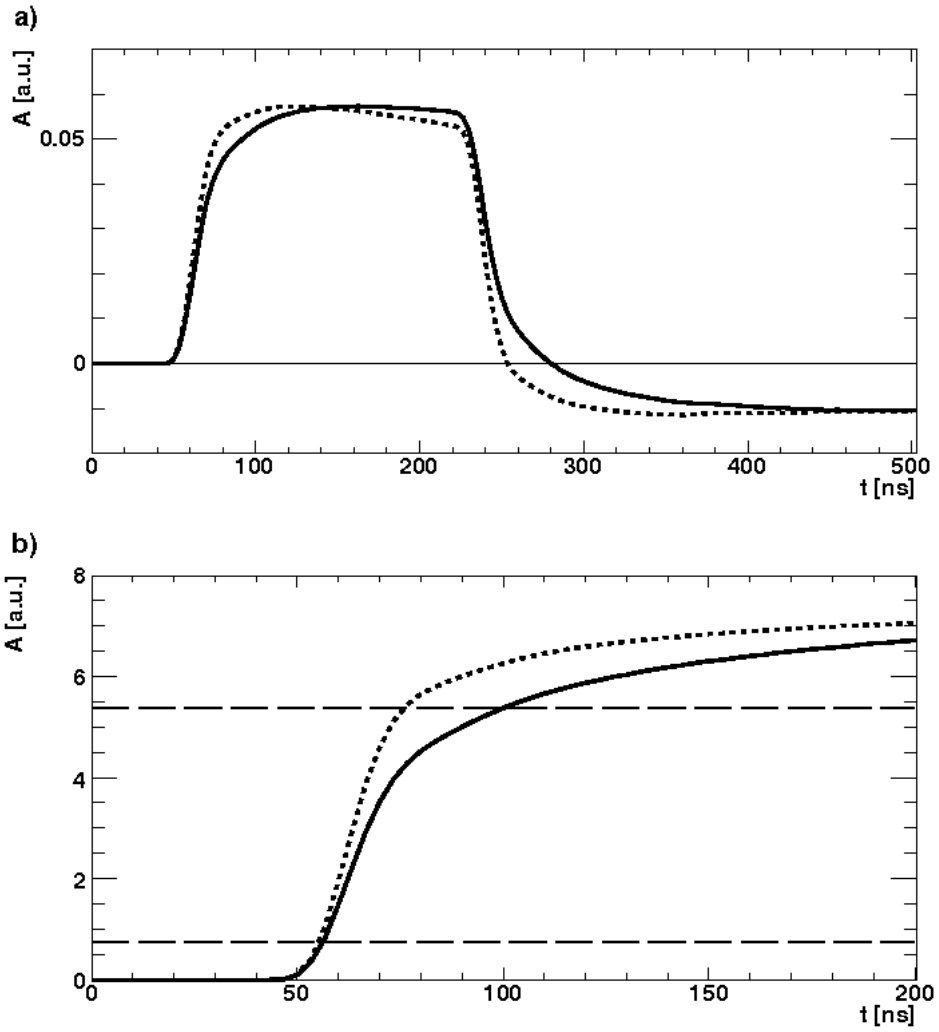

Fig. 6. Processed average pulses from fig. 1. a) Difference in ZCO time for a γ-ray pulse (short-dashed) and a neutron (solid) pulse. b) Difference between the integrated rise time of a γ ray (short-dashed) and a neutron (solid) pulse. The points at 10 % and 72 % of the pulse height are indicated by long-dashed lines.

by letting $w(t)$ be a step function, with a constant value in the time range t_1 to t_2, corresponding to the slow component, and 0 elsewhere. The parameters of the slow component algorithm are the start ($t = 0$) and end ($t = T$) of the pulse and the times t_1 and t_2, of which t_1 is most crucial, see fig. 7. The parameters were determined in the following way. A digital LED, as described in subsection 4.1, was implemented and used for determination of $t = 0$. The threshold of this discriminator was set to a very low value of about $E_\mathrm{e} = 5$ keV ($E_\mathrm{p} = 150$ keV), that is lower than the hardware CFD threshold in order not to loose any pulses. For t_2 and T an identical value of 533 ns was chosen. For times later than this value the pulse is barely above noise and contains very little information. The chosen value of t_1 was 33 ns, a value which was obtained by careful optimization of the figure-of-merit of the NGD (see subsection 4.6).

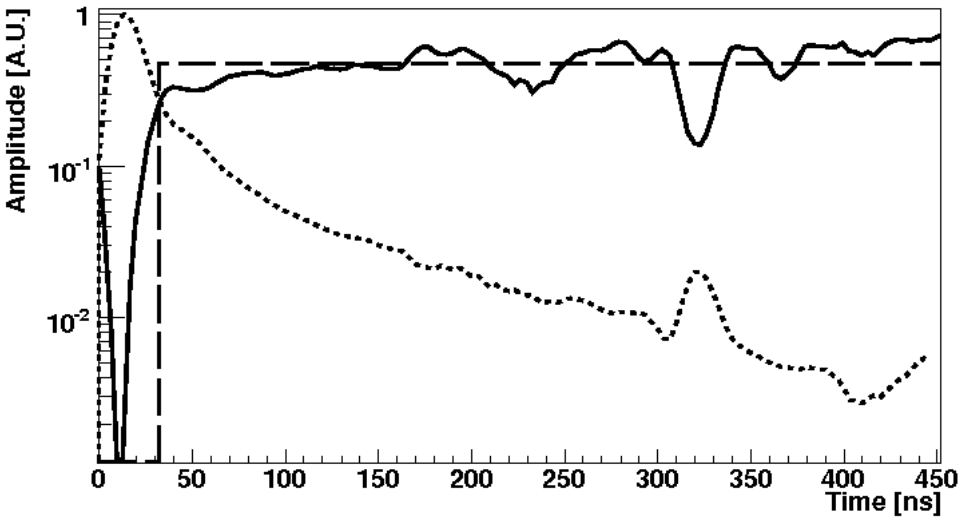

Fig. 7. Weighting function $w(t)$ of the GDM integral (solid) and slow component (dashed) algorithms shown together with an average neutron pulse (short-dashed).

For the actual NGD based on the slow component algorithm, the value of the observable S (see eq. 4) was evaluated as a function of the amplitude of the input pulse (see section 5).

The analogue version of the CC method is very similar to the digital slow component algorithm described here. In the analogue CC method the pulse is split and fed into two charge sensitive ADC channels. In the ADC's the charges corresponding to the fast and slow components are integrated by applying suitable gates at the times $t = 0$ to $t = t_1$ and $t = t_1$ to $t = t_2$, respectively. In practice the gates are usually set on the slow and total components of the pulse.

4.5 CC: GDM algorithm

By taking advantage of the digital signal processing, one may choose another, hopefully better, weighting function $w(t)$, than the simple step function used in the slow component algorithm. The weighting function can be evaluated directly from eq. 5. This was done by making use of the TOF parameter, by which neutrons and γ rays also could be discriminated. Average γ-ray and neutron pulses were created by selecting all pulses with a TOF value of $\pm 1\sigma$ from the maxima in the γ-ray and neutron TOF distributions, respectively. A total of about 70 000 γ-ray and 40 000 neutron pulses were used for making the average pulses and these are shown in fig.1. The same digital leading edge discriminator and threshold as in the slow component algorithm was used to define the start of the pulse ($t = 0$). The length of the pulse was also

the same, i.e. $T = 533$ ns. The created average pulses were then treated in accordance with eq. 5 to get the optimal weighting function $w(t)$, shown in fig. 7. In the analysis, each sampling point of a pulse $p(t)$ was multiplied by the corresponding weight $w(t)$, and these products were summed together to form the observable S according to eq. 5. The observable S will be referred to as the GDM integral [28], S_{GDM}. The GDM integral is usually normalized to the amplitude, A, of the pulse (see below).

4.6 Figure-of-merit parameters

In order to quantify the results of the NGD, two different figure-of-merit (FOM) parameters were defined. One of the most common definitions [29] of a FOM in this context is

$$M = \frac{|X_\gamma - X_n|}{W_\gamma + W_n}. \tag{12}$$

This is a unit-less ratio of the difference between the peak positions X_i divided by the sum of their FWHM, W_i ($i = \gamma, n$). The parameters X_i and W_i are obtained from a distribution of the used NGD parameter, e.g. ZCO time, the S observable, or even TOF. An increased value of M corresponds to a a better NGD. The FOM parameter M is usually determined by fitting two Gaussian or similar functions to the distribution of the NGD parameter. The fitting method works well if the distributions have well defined forms. This is usually not the case and therefore the following method, which does not require any fitting, was developed and used. Pulses due to neutrons and γ rays were separated by making cuts on the TOF parameter. The selected widths of the cuts were $\pm 2\sigma$ around the maxima of the neutron and γ-ray TOF distributions, which gave a clean enough selection. Two separate distributions of the NGD parameter under evaluation were created, one with a TOF cut on neutrons, the other with a TOF cut on γ rays. These distributions had only a single peak corresponding to neutrons and γ rays, respectively. The parameters X_i and W_i could then easily and directly be extracted (without fitting) from the distributions as the maximum and FWHM of the distributions, respectively. This procedure is illustrated in fig. 8 for NGD with the GDM algorithm.

The FOM parameter M does not take into account any effects of bad NGD due to random events or pile-up of several close lying pulses in the liquid scintillator detector. A mis-identification of neutrons as γ rays, or vice versa, due to such effects may be of great nuisance in real experiments, in particular when the detector rates are high or when the ratio of number of detected neutrons to γ rays is very small. For example, an increase of the distance $|X_\gamma - X_i|$ between peaks, which already are well separated in the distribution

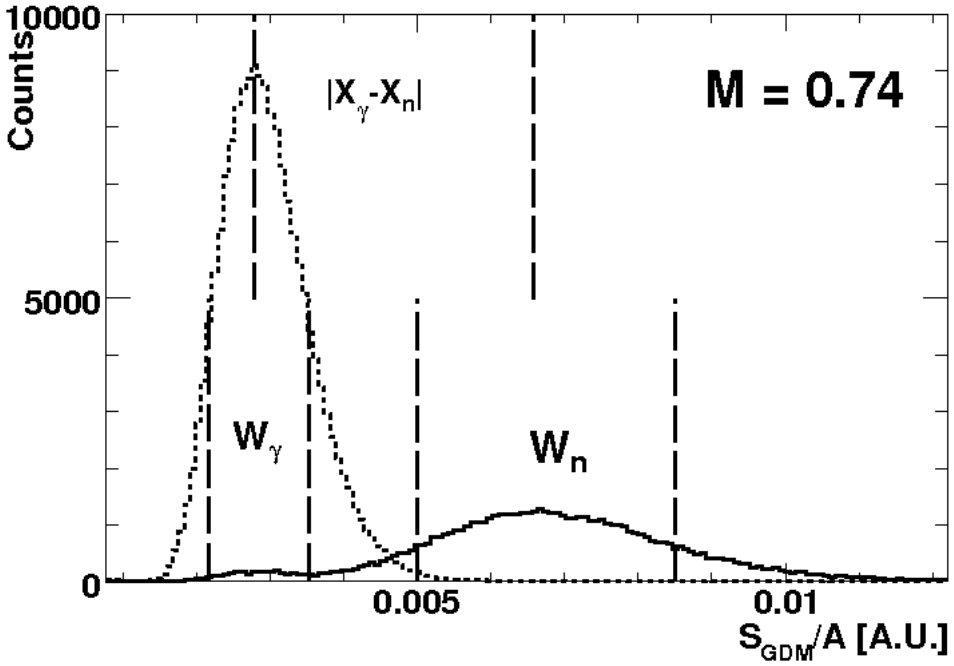

Fig. 8. Illustration of the extraction of the parameters $X_\gamma, X_n, W_\gamma, W_n$, which are needed for evaluation of the FOM parameter M. Neutrons (solid line) and γ rays (short dashed line) were selected by making cuts on the TOF parameter (see text). The amplitude of the pulses shown in this figure are in the range E_e = 100-115 keV for electrons, which corresponds to E_p = 760-830 keV for recoil protons.

of an NGD parameter, will increase M. However, the amount of neutrons misidentified as γ rays, due to random and pile-up effects, will in this case usually be the same even if M has increased.

Another drawback of using the standard FOM parameter M is that it can only be extracted from one dimensional data, i.e. from a distribution of just one NGD parameter. In the analysis of data obtained in real experiments, correlations between several NGD parameters are usually evaluated. Another FOM parameter, which quantifies the NGD, including random and pile-up effects, and which can be used also in two dimensions, was therefore defined as follows.

Two dimensional (2D) cuts on the TOF parameter versus the evaluated NGD parameter were applied. This is illustrated in fig. 9a, which shows a 2D histogram of the TOF versus the S_GDM/A parameter for pulses of amplitude E_e = 500-700 keV. In this plot, the centroid of the prompt γ-ray distribution, which contains most of the events, is located at TOF $\sim$ 110 ns and $S_{\mathrm{GDM}/A} \sim 0.003$. The neutron events are centred at TOF $\sim$ 140 ns and $S_{\mathrm{GDM}/A} \sim 0.0055$. Random TOF events, due to the detection of γ rays or neutrons from two different ^{252}Cf decays (or background γ rays) in the BaF_2

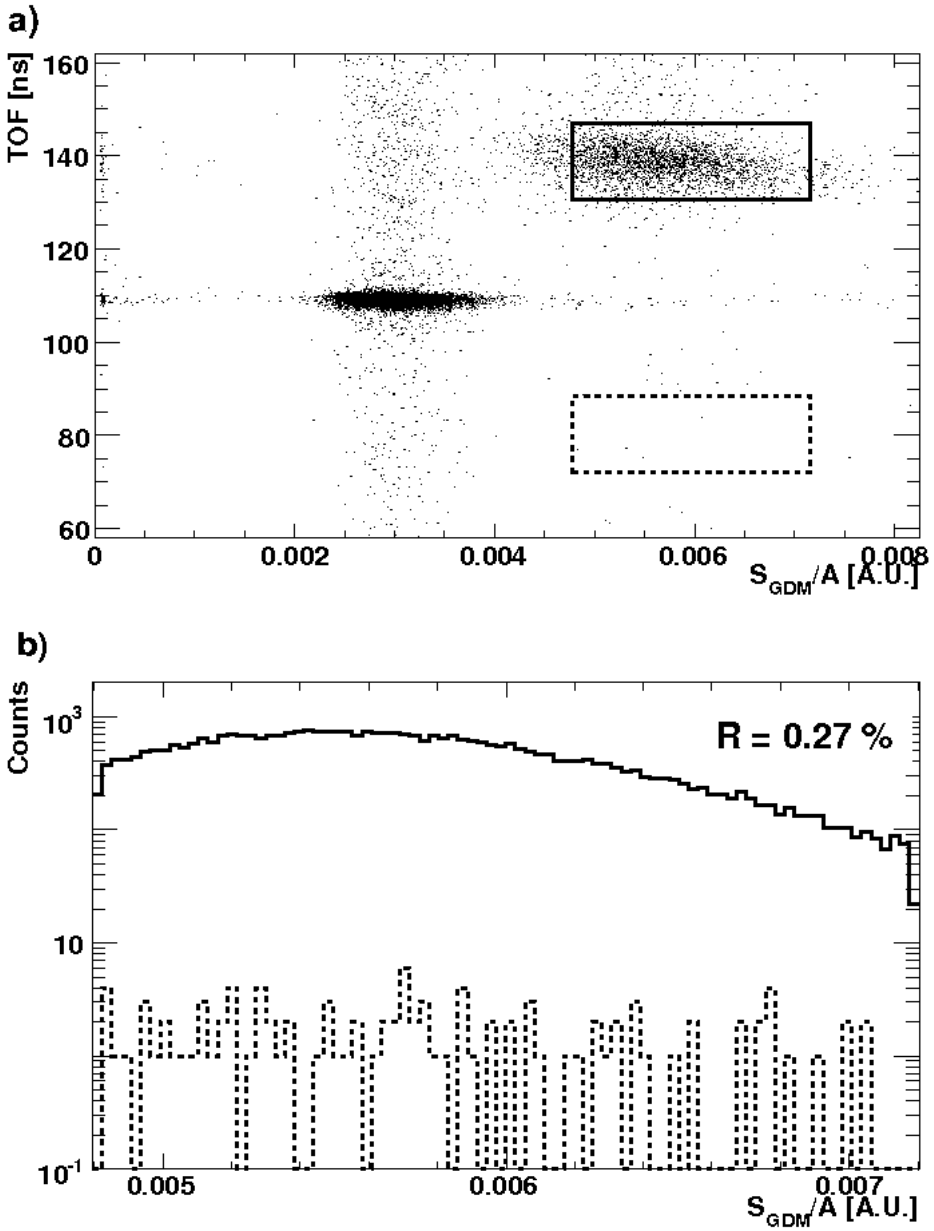

Fig. 9. a) TOF versus S_{GDM}/A with gates on neutron (rectangle with solid lines) and background (dashed lines) events. b) Projection on the S_{GDM}/A axis of the counts inside the solid and dashed rectangles in panel a). The amplitude of the pulses shown in this figure have an energy in the range $E_{\mathrm{e}} = 500$-700 keV for electrons, which corresponds to $E_{\mathrm{p}} = 2.2$-2.7 MeV for recoil protons.

and neutron detectors, are distributed anywhere parallel to the TOF axis. Some of the random γ rays can be seen as a vertical band of counts centred at a S_{GDM}/A value of ~ 0.003. Pile-up events in the neutron detector may have any S_{GDM}/A value, which is most clearly seen for the prompt γ rays as the horizontal band of counts centred at TOF ~ 110 ns. Simultaneous random and pile-up events are homogeneously distributed anywhere in the 2D histogram,

including inside the neutron distribution.

A 2D cut on the neutrons was set as shown by the rectangle with solid lines in fig.9a. The width of the cut on the TOF parameter was chosen to contain all counts within $\pm 2\sigma$ from the maximum of the neutron TOF distribution, while the width of the cut on the evaluated NGD parameter (S_{GDM}/A in fig. 9) was one FWHM on the left side and two FWHM on the right side. A 2D cut on background events, due to random coincidences and pile-up, was selected as shown by the rectangle with dashed lines in fig.9. For the NGD parameter the position of the background cut was identical to the position used for the neutron cut, while for the TOF parameter it was located at the same distance from the centroid of the prompt γ-ray distribution, but at a time before instead of after this centroid. By this choice, it was assumed that the neutron cut on average contains as many background events as the cut on background. Projections of the cuts on the S_{GDM}/A are shown in fig. 9b.

The new FOM parameter for quantifying the NGD was defined as the ratio of the number of counts in the background (N_{b}) and neutron (N_{n}) cuts:

$$R = \frac{N_{\mathrm{b}}}{N_{\mathrm{n}} - N_{\mathrm{b}}}. \tag{13}$$

A small value of R indicates a good discrimination of real neutron events from any other events. It should be stressed that the parameter R only is useful for comparing how well different NGD algorithms can discriminate neutrons from γ rays for analyses of the same experimental data set. Two data sets with differences in the relative number random or pile-up events will give different values of R even if the applied NGD algorithm is identical.

5 Analysis and results

5.1 Comparison of neutron-γ discrimination algorithms

A comparison of the NGD achieved with the digital PSD algorithms and with the analogue setup are shown in figures 10 and 11. Qualitatively the digital algorithms show similar NGD properties as what was achieved with the analogue data.

The FOM parameters M and R were evaluated for all digital algorithms and for the analogue data as a function of the amplitude of the pulses. The obtained results are shown in fig. 12. The expected increase of M and decrease of R with increasing amplitude is clearly visible in the figure. In general, the differences

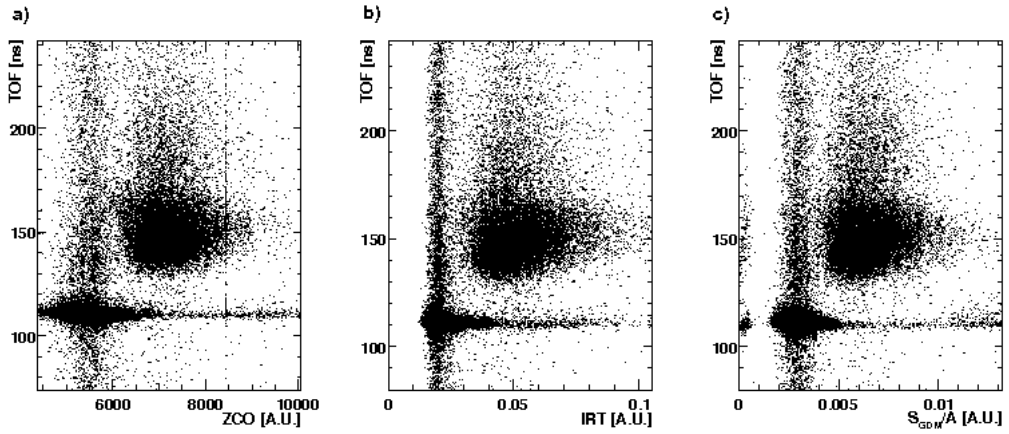

Fig. 10. Qualitative view of the neutron and γ-ray separation against TOF in the energy range $E_{\mathrm{e}} = 90$-700 keV, $E_{\mathrm{p}} = 730$-2700 keV for the: a) analogue separation, b) integrated rise time, c) GDM integral.

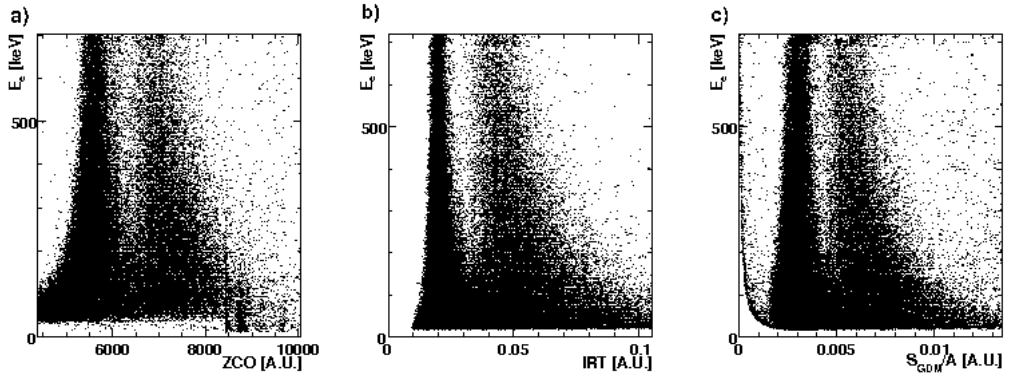

Fig. 11. Qualitative view of the neutron and γ-ray separation against E_{e} for the: a) analogue separation, b) integrated rise time, c) GDM integral.

in the obtained FOM parameters for the different algorithms, are rather small. All digital algorithms give at least as good or better FOM parameter than was obtained with the analogue data. The IRT algorithm based on the ZCO method gives the best M values (see fig. 12a). The convolution algorithm gives somewhat worse values of both M and R (fig. 12a and c) for pulses with amplitudes in the energy range $E_{\mathrm{e}} \simeq 40$-100 keV.

5.2 ADC sampling frequency and bit resolution

A detailed investigation of the performance of the IRT (based on the ZCO method) and GDM (CC method) algorithms as a function of the sampling frequency and bit resolution of the ADC was performed as described in this subsection.

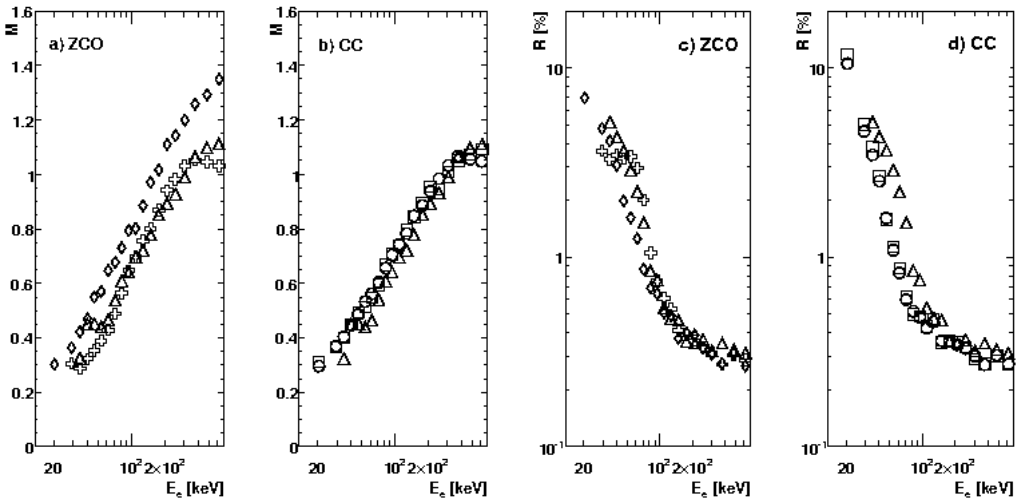

Fig. 12. Figure-of-merit parameters for the four algorithms: convolution (crosses), integrated rise time (diamonds), slow component (circles) and GDM integral (squares), together with the analogue pulse shape discrimination (triangles). a) M vs E_{e} for the two ZCO algorithms, b) M vs E_{e} for the two CC algorithms, c) R vs E_{e} for the two ZCO algorithms and d) R vs E_{e} for the two CC algorithms. Statistical and systematical errors are about the same or smaller than the size of the symbols.

From the gain and time matched event-by-event data new data sets were created with a reduction of either the bit resolution or the sampling frequency. The new data sets were then analysed with the same code as what was used for the original data set.

The bit reduction was achieved by performing an integer division by 2^{14-b} of the value of each sampling point value, where b is the number of bits in the new data set. The resulting value was then multiplied by the same factor. This made it possible to use exactly the same code for the analysis of all different data sets, because there was no need for corrections like rescaling of threshold values, etc. A total of 10 data sets with bit resolutions from 5 to 14 bits were created. The sampling frequency was lowered by removing a number of data points from the 300 Ms/s data set, resulting in new data sets corresponding to sampling frequencies of 150, 100, 75, 60 and 50 Ms/s. In addition a data set with 200 Ms/s was available from the measurement with the analogue PSD unit as described in section 3. Thus, a total of 7 data sets with samplings frequencies from 50 to 300 Ms/s, were created. The results obtained using the IRT and GDM algorithms for pulses of three different amplitude ranges are presented in fig. 13.

As seen in fig. 13a, both algorithms show a clear saturation of the FOM parameter M when the bit resolution is increased above a certain value. The point of saturation is almost independent of the amplitude of the pulses and

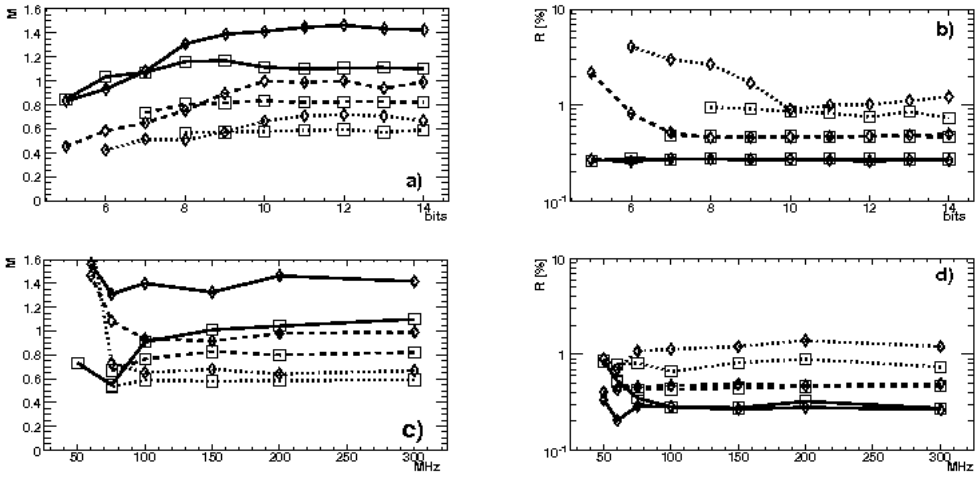

Fig. 13. The FOM parameters M (panel a and c) and R (b, d) as a function of ADC bit resolution (a, b) and sampling frequency (c, d). Results are shown for the algorithms of type IRT (diamonds; ZCO method) and GDM (squares; CC method). Pulses in three different energy ranges are shown: E_{e} = 50-70 keV, E_{p} = 500-540 keV (dotted), E_{e} = 115-135 keV, E_{p} = 830-920 keV (dashed), E_{e} = 500- 700 keV, E_{p} = 2200-2700 keV (solid). Statistical and systematical errors are about the same or smaller than the size of the symbols.

occurs at about 9 bits for the GDM algorithm and at about 10 bits for the IRT algorithm. The minimum required bit resolution depends, however, strongly on the requested dynamic range of the amplitudes of the pulses. In this work the dynamic range was E_{e} = 15-700 keV (E_{p} = 250-2700 keV), which is much smaller than what commonly is used in real experiments. A rescaling of the dynamic range from the one presently used to more reasonable values is shown in table 2. A dynamic range corresponding to a maximum energy deposit of E_{e} = 5.6 MeV (E_{p} = 12 MeV), which requires a bit resolution of 12 bits, seems adequate in most experiments.

The dependency of the FOM parameter R on the bit resolution is shown in fig. 13b. The two algorithms give very similar results for the intermediate and high energy pulses, while the IRT algorithm gives slightly better R values for the low energy pulses. In contrast to the results obtained for the M parameter (panel a), there is an energy dependency of the bit resolution value at which the R parameter saturates. For the low energy pulses, R saturates at a bit resolution of ≥ 9 bits and ≥ 10 bits for the IRT and GDM algorithms, respectively. For the intermediate energy pulses both algorithms saturate at ≥ 7 bits, while no saturation point was observed for the high energy pulses for bit resolutions of 5 bits and higher. No M and R values could be obtained for the small and intermediate amplitude pulses at the lowest bit resolutions.

The results obtained for different sampling frequencies are shown in fig. 13c and d, regarding the M and R parameters, respectively. In general one can

Table 2
The dependency of the maximum electron energy E_e and corresponding recoil proton energy E_p on the ADC bit resolution, with retained saturated (best) value of the FOM parameter M shown in fig. 13a.

Nr of bits	Integrated rise time (ZCO)		GDM integral (CC)	
	E_e [MeV]	E_p [MeV]	E_e [MeV]	E_p [MeV]
9	0.70	2.7	0.35	1.7
10	1.4	4.4	0.70	2.7
11	2.8	7.3	1.4	4.4
12	5.6	12	2.8	7.3
13	11	-	5.6	12
14	22	-	11	-

say that there is no strong dependency of M and R on sampling frequency. The M values saturate and become more or less constant above 100 Ms/s, except for the high energy pulses treated by the GDM algorithm, in which case M increases slowly above 100 Ms/s. No M values could be evaluated for the intermediate and low energy pulses with the IRT algorithm below 75 Ms/s, which apparently does not work so well below this sampling frequency for pulses with smaller signal to noise ratio. The R values saturate for sampling frequencies already above about 75 Ms/s. The apparently odd frequency behaviour for low-energy pulses is due to asymmetries in the neutron and γ-rays distributions and does not imply a better NGD.

5.3 Time resolution at 100 Ms/s

In a fully digital NGD system an external TAC, as used in this work, will not be available. For the TOF measurement, the starting time of the pulse in the neutron detector must instead be determined from the digitized waveform itself. A test of the influence of the finite sampling frequency on the achievable time resolution was made in the following way. A timing parameter was extracted from the digitized waveforms of the TNT2 channels 1 and 2, each recorded with a sampling frequency of 100 Ms/s. The waveforms were integrated as described in subsection 4.3 and a LED (see subsection 4.1) with a threshold set at half of the amplitude of the integrated pulse, was applied. Pulses of all amplitudes were used in the analysis. The timing parameter Δt_{21} was created by taking the difference between the extracted LED times of each of the two channels. The distribution of Δt_{21} is shown in fig. 14. The FWHM of the distribution is 1.7 ns, which is the contribution of the finite sampling

frequency (100 Ms/s in this case), to the total FWHM. The achievable intrinsic time resolution of a liquid scintillator detector plus PMT is typically FWHM = 1.5 ns or larger. With the present data it was not possible to perform the analysis at higher sampling frequencies, but it is expected that the FWHM will decrease linearly with increasing sampling frequency. Thus, already at 200 Ms/s the contribution of the finite sampling frequency to the total FWHM of the time resolution is almost negligible.

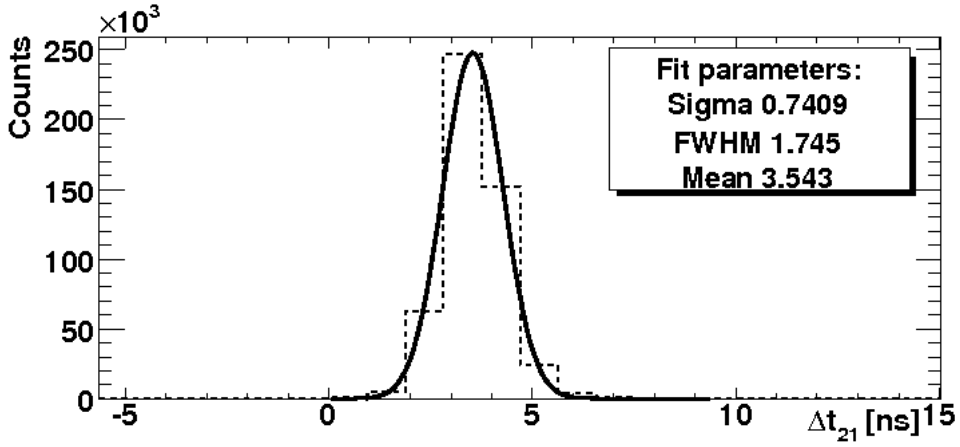

Fig. 14. Distribution of the time difference extracted from two waveforms recorded at 100 Ms/s. See text for details.

6 Summary and conclusions

In this work four different digital pulse-processing algorithms for discrimination of neutrons and γ rays in a liquid scintillator detector have been developed and compared to each other and to data obtained with an analogue neutron-γ discrimination unit. Two of the digital algorithms were based on the charge comparison method, while the analogue unit and the other two digital algorithms were based on the zero-crossover method. Two different figure-of-merit parameters, which quantifies the neutron-γ discrimination properties, were evaluated. All of the digital algorithms gave similar or better figure-of-merit values than what was obtained with the analogue setup.

A detailed study of the discrimination properties as a function of sampling frequency and bit resolution of the ADC was performed. The general conclusion is that an ADC with a bit resolution of 12 bits and a sampling frequency of 100 Ms/s is adequate for achieving an optimal neutron-γ discrimination for pulses having a dynamic energy range of 0.02 - 5.6 MeV and 0.3 - 12 MeV for γ rays and neutrons, respectively. The influence of a finite sampling frequency on the time resolution was also investigated. A FWHM of 1.7 ns was obtained at 100 Ms/s.

In order to further increase the quality of the neutron-γ discrimination it is necessary to handle random and pileup effects in an adequate way. Such effects will become more problematic in experiments using very high-intensity stable or high-intensity radioactive beams, in which an increased γ-ray background radiation is present. For such experiments it will be necessary to further develop the digital pulse-shape algorithms for rejection or recovery of pulses which are distorted

Acknowledgements

We are grateful to J. Ljungvall for the TNT2 library and to H. Mach for supplying the BaF_2 detector. This work was partially supported by the Swedish Research Council.

References

[1] Z. Podolyák, Int. J. Mod. Phys. E 15 (2006) 1967–1977.

[2] B. Rubio, Int. J. Mod. Phys. E 15 (2006) 1979.

[3] B. Rubio, T. Nilsson, Nucl. Phys. News 16 (1) (2006) 9.

[4] W. F. Henning, J. Phys. G Nucl. Partic. 34 (2007) 551.

[5] M. Lewitowicz, AIP Conference Proceedings 891 (2007) 91.

[6] P.-A. Söderström, Proceedings of International School of Physics "Enrico Fermi" course CLXIX - Nuclear structure far from stability: New physics and new technology, 2008, in print.
arXiv:0712.2166 [nucl-ex]

[7] S. E. Arnell, et al., Nucl. Instr. and Meth. A 300 (1991) 303.

[8] Ö. Skeppstedt, et al., Nucl. Instr. and Meth. A 421 (1999) 531.
http://nsg.tsl.uu.se/nwall/

[9] D. G. Sarantites, et al., Nucl. Instr. and Meth. A 530 (2004) 473.

[10] J. Cederkäll, et al., Nucl. Instr. and Meth. A 385 (1997) 166.

[11] J. Ljungvall, et al., Nucl. Instr. and Meth. A 528 (2004) 741.

[12] Saint-Gobain Crystals, France, BC501A data sheet.

[13] F. T. Kuchnir, F. J. Lynch, IEEE Trans. Nucl. Sci. NS-15 (3) (1968) 113.

[14] G. Knoll, Radiation Detection and Measurements, 3rd Edition, Wiley, 1999.

[15] J. B. Birks, The Theory and Practice of Scintillation Counting, Pergamon, 1964.

[16] T. K. Alexander, F. S. Goulding, Nucl. Instr. and Meth. 13 (1961) 244.

[17] M. Roush, et al., Nucl. Instr. and Meth. 31 (1964) 112.

[18] F. D. Brooks, Nucl. Instr. and Meth. 4 (1959) 151.

[19] D. Wolski, et al., Nucl. Instr. and Meth. A 360 (1995) 584.

[20] N. V. Kornilov, et al., Nucl. Instr. and Meth. A 497 (2003) 467.

[21] S. Marrone, et al., Nucl. Instr. and Meth. A 490 (2002) 299.

[22] B. D'Mellow, et al., Nucl. Instr. and Meth. A 578 (2007) 191.

[23] M. D. Aspinall, et al., Nucl. Instr. and Meth. A 583 (2007) 432.

[24] The TNT2 was designed and built by P. Medina, et al. at IPHC, Strasbourg. Presently it is available commercially from CAEN as model N1728.

[25] J. H. Friedman, Proceedings of the 1974 CERN School of Computing, 1974, p. 271.

[26] The NDE202 was built by D. Wolski, M. Moszyński, et al. at The Andrzej Soltan Institute for Nuclear Studies, Swierk, Poland.

[27] R. A. Cecil, et al., Nucl. Instr. and Meth. 161 (1979) 439.

[28] E. Gatti, F. D. Martini, Proceedings of International Conference at Belgrade, Vol. II, IAEA, 1962, p. 265.

[29] R. A. Winyard, et al., Nucl. Instr. and Meth. 95 (1971) 141.

[30] G. Ranucci, Nucl. Instr. and Meth. A 354 (1995) 389.